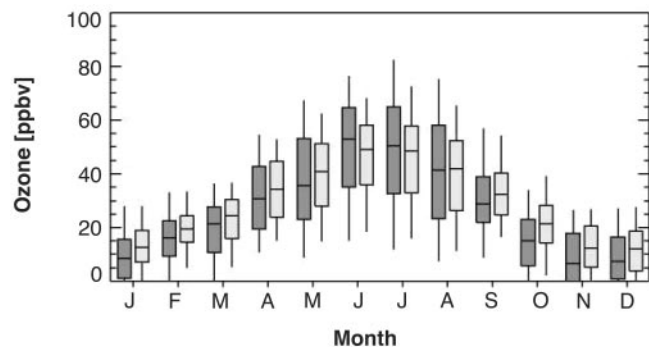


Fig. 4. Simulated seasonal cycle of surface ozone (in ppbv) at an arbitrary model grid box in Germany ("Frankfurt/Main") for present-day emissions (gray) and for the L3 hydrogen economy scenario (white). Each symbol represents the multiannual monthly statistics, with boxes denoting the central 50% of the data, whiskers showing the central 90%, and horizontal lines displaying the median concentration. Note the significant reduction of the high ozone values in summer.



logical options for generating and using molecular hydrogen. Clearly, more work is needed to derive more robust emission scenarios for realistic technological and economic projections. The most critical parameters with respect to the atmospheric implications of large-scale hydrogen use appear to be the associated changes in methane and NO_x emissions. The possible reduction in NO_x emissions would lead to reduced tropospheric ozone formation but also to a substantial degradation of the atmospheric oxidizing power, which could further aggravate climate forcing caused by methane and other greenhouse gases.

References and Notes

1. *Climate Change 2001: The Scientific Basis*, Contribution of Working Group I to the Third Assessment Report of the Intergovernmental Panel on Climate Change (Cambridge Univ. Press, Cambridge, 2001).

2. *Scientific Assessment of Ozone Depletion*, Report No. 47, World Meteorological Organization Global Ozone Research and Monitoring Project (World Meteorological Organization, Geneva, 2002).
3. J. A. Logan *et al.*, *J. Geophys. Res.* **104**, 26373 (1999).
4. A. Volz-Thomas *et al.*, in *Towards Cleaner Air for Europe—Science, Tools, and Applications*, Results from the Eurotrac-2 Synthesis and Integration Project, Part I (Magraf, Weikersheim, Germany, 2003), pp. 73–122.
5. World Health Organization, Fact Sheet No. 187 (September 2000) (available at www.who.int/inf-fs/en/fact187.html).
6. W. Zittel, M. Altmann, in *Proceedings of the 11th World Hydrogen Energy Conference*, Stuttgart, Germany, June 1996 (Schön & Wetzel, Frankfurt am Main, Germany, 1996), pp. 71–82.
7. This "less than 0.1%" figure was given in personal communications with an employee from the former pipeline operator, Hüls A. G., in 1990.
8. J. Gretz, B. Drolet, D. Kluysskens, F. Sandmann, O. Ullmann, in *Proceedings of the 9th World Hydrogen Energy Conference*, Paris, France, 22 to 25 June 1992 (M.C.I. Manifestations et Communications Internationales, Paris, France), pp. 1821–1822.

9. I. J. Oonk, M. E. J. P. Vosbeek, *Methane Emissions Due to Oil and Natural Gas Operations in The Netherlands*, Final Report, TNO Milieu, Energie en Procesinnovatie, R95-168 (TNO, Apeldoorn, Netherlands, 1995).
10. P. C. Novelli *et al.*, *J. Geophys. Res.* **104**, 30427 (1999).
11. D. A. Hauglustaine, D. H. Ehhalt, *J. Geophys. Res.* **107**, 4330 (2002).
12. T. K. Tromp, R.-L. Shia, M. Allen, J. M. Eiler, Y. L. Yung, *Science* **300**, 1740 (2003).
13. L. W. Horowitz *et al.*, *J. Geophys. Res.* **108**, 10.1029/2002JD002853 (2003).
14. C. Granier, personal communication.
15. This scenario is roughly consistent with a 100% transition of all mobile combustion engines to fuel cell technology. In the model, we reduced only CO and NO_x emissions, which are expected to have the largest impact.
16. J. A. Logan, M. J. Prather, S. C. Wofsy, M. B. McElroy, *J. Geophys. Res.* **86**, 7210 (1981).
17. M. Prather *et al.*, *Geophys. Res. Lett.* **30**, 1100 (2003).
18. J. G. J. Olivier, J. J. M. Berdowski, in *The Climate System*, J. Berdowski, R. Guicherit, B. J. Heij, Eds. (A. A. Balkema/Swets & Zeitlinger, Lisse, Netherlands), pp. 33–78 (2001) (data are available at www.rivm.nl/env/int/coredata/edgar/).
19. In our model, we cannot fully evaluate the change in CH₄ concentration associated with the increased CH₄ lifetime, because we use prescribed surface concentrations rather than emission fluxes as boundary conditions. Simulation L3CH4, with surface methane concentrations increased by 10%, should therefore be a good approximation of the combined effects.
20. We thank C. Granier for providing us the year 2000 emissions data, D. Ehhalt for helpful discussions, and the reviewers for helpful comments. M.G.S. acknowledges funding from the German AFO2000 program under contract 07ATF39.

23 July 2003; accepted 24 September 2003

Discovery of Olivine in the Nili Fossae Region of Mars

Todd M. Hoefen,^{1*} Roger N. Clark,¹ Joshua L. Bandfield,² Michael D. Smith,³ John C. Pearl,³ Philip R. Christensen²

We have detected a 30,000-square-kilometer area rich in olivine in the Nili Fossae region of Mars. Nili Fossae has been interpreted as a complex of grabens and fractures related to the formation of the Isidis impact basin. We propose that post-impact faulting of this area has exposed subsurface layers rich in olivine. Linear mixture analysis of Thermal Emission Spectrometer spectra shows surface exposures of 30% olivine, where the composition of the olivine ranges from Fo₃₀ to Fo₇₀.

The Mars Global Surveyor (MGS), carrying the Thermal Emission Spectrometer (TES), arrived at Mars on 11 September 1997 (1). One of the primary goals of the TES experiment is to map and determine the composition of martian surface materials (2, 3). The TES instrument collects spectra, using a Michelson interferometer,

from 1650 to 200 cm⁻¹ (wave numbers) with spectral sampling of 5.3 cm⁻¹ with a 6.25 cm⁻¹ bandwidth (full width at half maximum) or 10.6 cm⁻¹ with a 12.5 cm⁻¹ bandwidth (full width at half maximum) (2–4). We combined TES data from multiple orbits into three-dimensional image cubes, with two spatial and one spectral dimension, and searched the resultant data set for spectral features that would allow us to identify surface mineralogy.

TES spectra are emission spectra that contain both atmospheric and surface components (5). Dust, CO₂, water ice aerosols, and water vapor absorptions are present in most

TES spectra. The atmospheric dust and CO₂ bands are typically the most dominant features, the strongest being the CO₂ band at 667 cm⁻¹. The depth of the strong dust band, near 1100 cm⁻¹, changes as a function of the dust load in the atmosphere. Water vapor bands are present in two regions in our spectral range: vibration rotation bands located between 1350 and 1600 cm⁻¹ and pure rotational bands located between 200 and 300 cm⁻¹.

Olivine [(Mg,Fe)₂SiO₄] is a greenish magnesium/iron orthosilicate common in many mafic rocks. It has a solid solution series ranging from forsterite, Mg₂SiO₄ (Fo₁₀₀) to fayalite, Fe₂SiO₄ (Fo₀) (6, 7). In most terrestrial environments, olivine is susceptible to chemical weathering and readily alters to iddingsite, goethite, serpentine, chlorite, smectite, maghemite, and hematite in the presence of water (8).

We compared spectra with a range of olivine compositions with our TES spectra. Included in the spectral feature comparison was a series of <60-μm Kiglapait (KI) olivine grains with Fo compositions that range from Fo₆₆ to Fo₁₁ and a suite of Hawaiian green sand beach olivine, samples GDS70a to GDS70e (Fo₈₉), with grain sizes of <30, <60, 60 to 104, 104 to 150, and 150 to 250 μm (9) (table S1).

¹U.S. Geological Survey, Denver, CO 80225, USA.
²Arizona State University, Tempe, AZ 85287, USA.
³Goddard Space Flight Center, Greenbelt, MD 20771, USA.

*To whom correspondence should be addressed. E-mail: thoefen@usgs.gov

REPORTS

Spectra from the laboratory-based measurements of the olivine suites show systematic variations in the position of the mid- and far-infrared spectral features (4). These variations correspond to differences in composition (Fig. 1). The olivine absorption bands between 16 and 50 μm shift toward shorter wavelengths as the amount of FeO in the olivine decreases. For example, in samples KI4143, KI3054, and GDS70, the position of the first SiO band shifts from 382 cm^{-1} (26.2 μm) to 400 cm^{-1} (25 μm) to 422 cm^{-1} (23.7 μm). Spectral measurements of the GDS70 olivine series show that decreasing the grain size does not shift the band position but does decrease band depths (Fig. 1) (10, 11).

To make a correct interpretation of surface mineralogy, it is important to account for and remove the effects of atmospheric constituents from TES spectral data. Spectrum ratio corrections, which can effectively cancel most of the atmospheric influence on the TES spectra, were applied. The spectrum ratio corrections included seven spectra that were selected and averaged, to re-

duce noise, from pixels that mapped as olivine in ock 2943 (12). We then selected and averaged several pixels from ock 2943 from an area just south of Nili Fossae that did not display any of the olivine absorptions. These sets of spectra were sufficiently close together that they had similar atmospheric and dust components, surface temperatures, and elevations. The averaged spectrum with the olivine features was divided by the averaged spectrum without olivine features, resulting in an atmospherically corrected ratioed spectrum or flat-field spectrum (Fig. 2). This method was used extensively on both 5 and 10 cm^{-1} data from the olivine-rich area. Another correction applied was the surface-atmosphere separation technique (13, 14), which uses a radiative transfer method to isolate surface and atmospheric components. The contributions of dust and other atmospheric components were calculated and removed from the spectrum. A third correction involved the removal of atmospheric CO_2 and H_2O gas absorption features from the spectrum of each pixel. Computed atmo-

spheric reference spectra were scaled to observed intensities by methods similar to those used in atmospheric removal algorithms for terrestrial imaging spectroscopy (15–17). The computed atmospheric reference spectra were derived from computer models of the martian atmosphere. Reference spectral features from the atmospheric models were fitted to those in the observed spectrum. The observed spectrum was then divided by the fitted reference spectra to remove the features. The corrected spectra allow the olivine features to be readily identified. In particular, spectral features centered at 345, 410, 520, and 925 cm^{-1} match features observed in the spectra of terrestrial olivines (Figs. 1 and 2).

TES data were assembled into image cubes that cover the planet from $\pm 60^\circ$ latitude. We used spectral feature mapping tools (18) to map surface mineralogy (4). We used the ~ 300 to ~ 550 cm^{-1} region extensively, because it provides a relatively clear spectral window through the martian atmosphere, with comparatively little influence from dust, CO_2 or H_2O gas, or ice clouds. This spectral region contains features from many minerals. Diagnostic spectral features chosen for each mineral were used to map the mineralogy of the martian surface. For olivine mapping, we used three spectral features between 300 cm^{-1} (33.3 μm) and 600 cm^{-1} (16.6 μm): the emittance minima near 400 cm^{-1} (25 μm), the spectral peak near 450 cm^{-1} (22.2 μm), and the emittance minima near 510 cm^{-1} (19.6 μm). For olivine to be identified by the mineral mapping technique described here, all three spectral features must be present. The diagnostic features from the spectral library were then compared to possible corresponding features in the TES image cubes. Those minerals with the best spectral match to the surface spectra were identified, and mineral maps were constructed.

We discovered olivine in small outcrops distributed nearly globally over the martian surface between $\pm 60^\circ$ latitude, but the largest surface exposure occurs in the Nili Fossae area. This region lies in the older, more cratered terrain northeast of the younger lava flows of Syrtis Major. A series of ring fractures occur in Nili Fossae that have been associated with the Isidis impact basin (19–21). The fracture and graben structures south of Nili Fossae have been partially buried by lava flows from Syrtis Major (19).

Based on the olivines in our spectral library, sample KI3054 (Fo_{66}) mapped the most area (to the most pixels), followed by KI189 (Fo_{60}) and KI4143 (Fo_{41}). Spatially, the southwestern region of Nili Fossae contains olivine with a compositional range of Fo_{60} to Fo_{70} , whereas the northeast region consists of olivine ranging from $<\text{Fo}_{40}$ to

Fig. 1. The shift in olivine feature positions as a function of olivine composition. As FeO in the olivine decreases, the bands shift toward shorter wavelengths. The red line is a TES spectrum from Nili Fossae. The black lines are laboratory spectra of olivines with different compositions. The KI samples are all <60 - μm samples. The GDS70.a and GDS70.d samples have grain sizes of 150 to 250 μm and <60 μm , respectively. The GDS70 spectra show that the band positions do not change with grain size. All spectra have been scaled to a similar relative emittance.

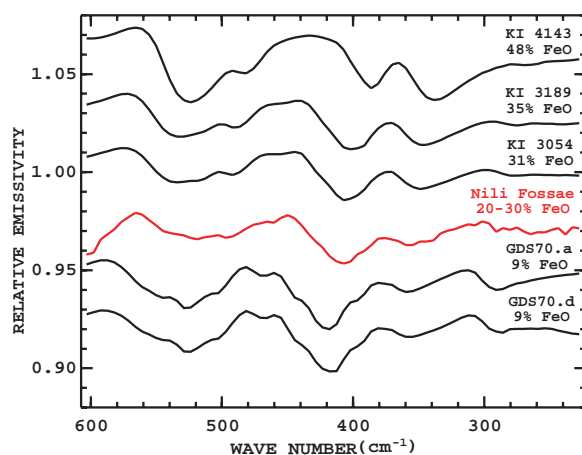
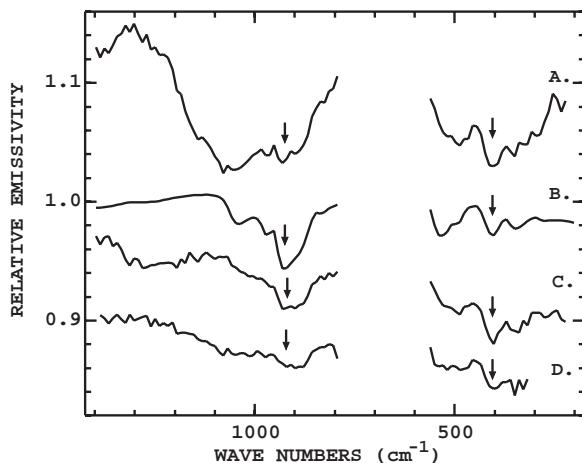


Fig. 2. MGS TES spectra from the olivine-rich areas in the Nili Fossae region are shown after the application of three methods of atmospheric removal. All methods reveal the same surface spectral features. Spectrum A has all atmospheric gas bands removed, leaving the dust and surface spectral features. Spectrum B shows a spectrum of olivine for comparison. Spectrum C shows the ratio of a spectrum that contains the olivine signatures to a spectrum from a nearby region that does not exhibit any olivine signatures. The ratio process removed atmospheric gas and dust absorptions. The surface-atmosphere-separation method (13) (Spectrum D) was used to remove atmospheric gas, dust, and water vapor bands. All three methods result in a cleaner surface spectrum that prominently shows the strong olivine features. The arrows point to the emittance minima near 900 and 400 cm^{-1} . The gap in the middle of the plot, from 600 to 800 cm^{-1} , is where CO_2 strongly absorbs, blocking signal from the surface.



Fo_{60} . Low-iron olivines did not map in the Nili Fossae region (Fig. 3). Another outcrop on the southeastern rim of Isidis mapped mostly as the KI3054 (Fo_{66}) olivine, followed by the KI4143 (Fo_{41}) and a few pixels of KI3189 (Fo_{60}). This range of olivine compositions is consistent with other data inferred from TES (22, 23) and also with the olivine-rich SNC (shergottite, nakhlite, and chassigny) meteorites (24). A variety of other minerals were searched for simultaneously with the olivine spectra, but no other minerals, except for a few pixels of hematite, showed spectral features strong enough to be identified with our spectral feature identification method in the Nili Fossae Region.

Linear mixture analysis (25) on spectra from rock 2943 revealed surface exposures that contain ~30% olivine. The other main minerals found in the deconvolution were plagioclase feldspar (17%) and pyroxene (17%). For the olivine estimate of 30%, we used an olivine spectrum with a 1-mm grain size (25). The spectral feature strength is roughly proportional to grain size in the 180- to 30- μ m size range, as observed in our olivine GDS70 (grain size) series. If the grain size is smaller than a couple of hundred microns, then the feature strengths will be proportionally weaker and corresponding abundances larger.

There are several possible origin scenarios and implications for this regional exposure of olivine. The Nili Fossae area could be underlain by an olivine-rich igneous lithology that has been directly exposed by Isidis basin tectonics, such as an ultramafic or mafic unit or a shallow intrusion similar to the lunar crater Copernicus (26). The Isidis impact site could have been the focal point of post-impact basaltic volcanism, from which olivine-rich basalt flowed onto the surface near Nili Fossae (Fig. 4). Another possibility could be post-impact faulting followed by erosion, exposing an olivine-rich layer.

Considering the geologic evidence, we believe that olivine was present in the subsurface before the Isidis impact. Faulting occurred after the impact, exposing subsurface layers that may have been rich in olivine. This implies the olivine could have been exposed at the surface since the time of the impact, which has been estimated to be of Hesperian age (27).

Olivine exposed to a warm and wet environment will alter to secondary minerals. Other than hematite, we have not been able to identify any of the other common alteration products of olivine in the TES data. Our observations of regional exposures of olivine could have implications for warm-wet periods in martian climatic history, if the age of the olivine could be constrained. Syrtis Major is thought to be ~3.6 billion years old (28), and because the Isidis impact basin is older

than Syrtis Major, we can deduce that Nili Fossae formed at least 3.6 billion years ago. This could be the upper limit to when the olivine was exposed at the surface. If the

olivine was exposed shortly after the impact event, the martian surface may have been dry and cold for more than 3 billion years, but if the olivine was recently uncovered at the

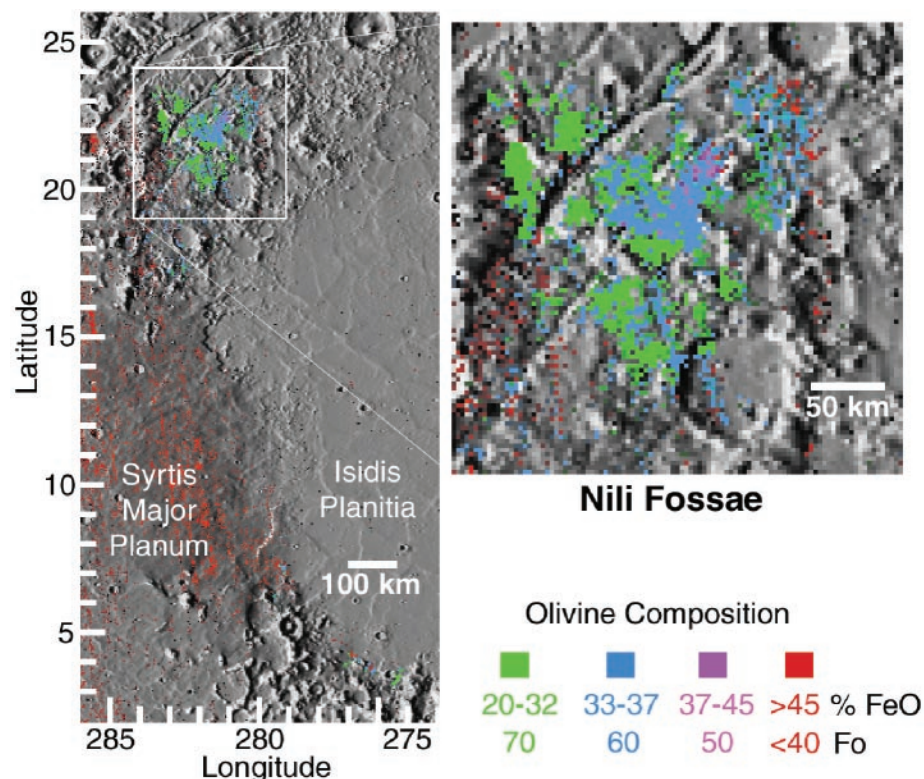


Fig. 3. Olivine composition mapped in the Nili Fossae region. There appears to be a trend toward higher FeO content (and lower Fo values) to the northeast. The enlarged square is ~280 km across. After counting the number of pixels that mapped as olivine in this region, we can say that the Nili Fossae olivine exposure covers ~30,000 sq. km.

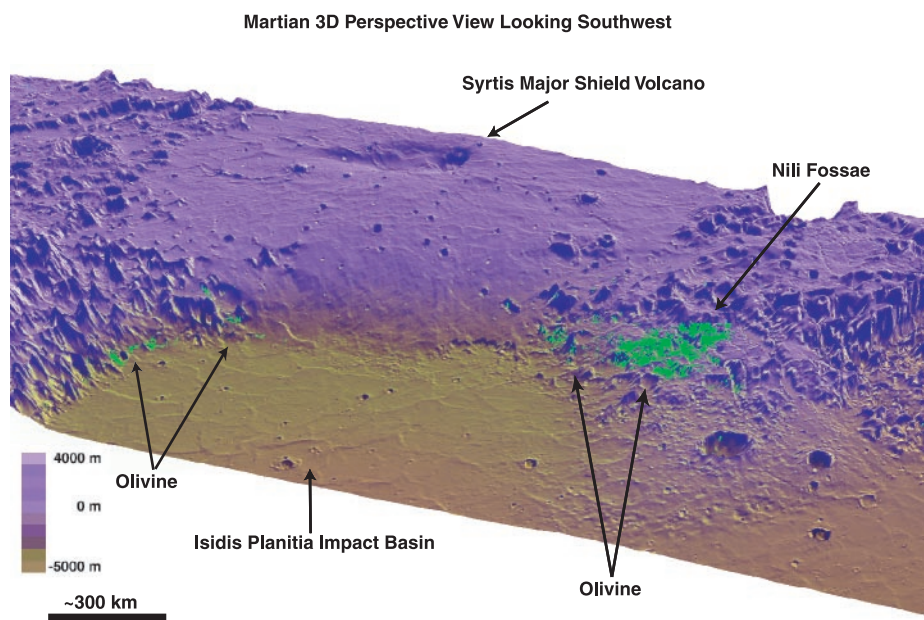


Fig. 4. This figure shows a three-dimensional perspective of Nili Fossae, Syrtis Major, and Isidis Planitia. This image was created by combining Mars Orbiter Laser Altimeter (MOLA) elevation data and TES spectral data. TES pixels that mapped as olivine are shown in green. MOLA elevation data is shown in the brown (lower elevations) and violet (higher elevations).

REPORTS

surface, then it could have been cold and dry for as little as a few thousand years. We have also mapped small olivine exposures on crater rims and central peaks in other areas that are of Noachian-Hesperian age. This may help the argument (29) that Mars has been cold and dry for a long period of time.

References and Notes

1. A. L. Albee, F. D. Palluconi, R. E. Arvidson, *Science* **279**, 1671 (1998).
2. P. R. Christensen *et al.*, *J. Geophys. Res.* **97**, 7719 (1992).
3. P. R. Christensen *et al.*, *Science* **279**, 1692 (1998).
4. Materials and methods are available as supporting material on Science Online.
5. Spectroscopy is defined as "the study of light as a function of wavelength that has been emitted, reflected, or scattered from a solid, liquid, or gas" (11).
6. W. A. Deer, R. A. Howie, J. Zussman, *Orthosilicates*, vol. 1A of *Rock Forming Minerals* (Longmans Green, London, ed. 2, 1963).
7. $\ln F_{O_x} = \frac{\text{mol \% Mg}}{(\text{mol \% Mg} + \text{mol \% Fe})} \times 100$
8. S. M. Colman, D. P. Dethier, Eds., *Rates of Chemical Weathering of Rocks and Minerals* (Academic Press, Orlando, FL, 1986), pp. 25–29.
9. T. V. V. King, I. Ridley, *J. Geophys. Res.* **92**, 11457 (1987).
10. R. N. Clark, in *Manual of Remote Sensing*, A. Rencz, Ed. (Wiley, New York, 1999), vol. 3, chap. 1.
11. J. W. Salisbury, L. S. Walter, N. Vergo, D. M. D'Aria, *Infrared (2.1–25 μm) Spectra of Minerals* (Johns Hopkins Univ. Press, Baltimore, MD, 1991).
12. An ock (Orbit Counter Keeper) is a TES orbit number from orbit insertion on 12 September 1997.
13. J. L. Bandfield, M. D. Smith, *Icarus* **161**, 47 (2003).
14. M. D. Smith, J. L. Bandfield, P. R. Christensen, *J. Geophys. Res.* **105**, 9589 (2000).
15. B. C. Gao, K. B. Heidebrecht, A. F. H. Goetz, *Remote Sens. Environ.* **44**, 165 (1993).
16. R. O. Green *et al.*, *Remote Sens. Environ.* **65**, 227 (1998).
17. R. N. Clark *et al.*, *AVIRIS Workshop Proceedings* (NASA Jet Propulsion Laboratory, Pasadena, CA, 2002) (available at <http://speclab.cr.usgs.gov/PAPERS.calibration.tutorial>).
18. R. N. Clark *et al.*, *J. Geophys. Res.*, in press.
19. E. R. Kraal *et al.*, *Proc. Lunar Planet Sci. Conf.* **29**, 1998.
20. W. K. McKinnon, H. J. Melosh, *Icarus* **44**, 454 (1980).
21. H. H. Kieffer, B. M. Jakosky, C. W. Snyder, M. S. Matthews, *Mars* (Univ. of Arizona Press, Tucson, AZ, 1992), p. 363.
22. P. R. Christensen, J. L. Bandfield, M. D. Smith, V. E. Hamilton, R. N. Clark, *J. Geophys. Res.* **105**, 9609 (2000).
23. V. E. Hamilton, P. R. Christensen, H. Y. McSween Jr., J. L. Bandfield, *Meteor. Planet. Sci.* **38**, 871 (2003).
24. V. E. Hamilton, P. R. Christensen, H. Y. McSween Jr., *J. Geophys. Res.* **102**, 25593 (1997).
25. J. L. Bandfield, *J. Geophys. Res.* **107**, 2001JE001510 (2002).
26. C. M. Pieters, D. E. Wilhelms, *J. Geophys. Res.* **90** (suppl.), C415 (1985).
27. W. K. Hartmann, G. Neukum, in *Chronology and Evolution of Mars*, R. Kallenbach, J. Geiss, W. K. Hartmann, Eds. (International Space Science Institute, Bern, 2001), pp. 165–194.
28. H. Hiesinger, J. W. Head III, *Proc. Lunar Planet Sci. Conf.* **32** (abstr. 1063), 2002.
29. P. R. Christensen *et al.*, *Science* **300**, 2056 (2003).
30. We thank T. V. V. King for the use of and insight into her olivine collection and Arizona State University and NASA for their support of our MGS TES research.

Supporting Online Material

www.sciencemag.org/cgi/content/full/302/5645/627/DC1

Materials and Methods
Table S1

References and Notes

25 July 2003; accepted 23 September 2003

LysM Domain Receptor Kinases Regulating Rhizobial Nod Factor–Induced Infection

Erik Limpens, Carolien Franken, Patrick Smit, Joost Willemse, Ton Bisseling,* René Geurts

The rhizobial infection of legumes has the most stringent demand toward Nod factor structure of all host responses, and therefore a specific Nod factor entry receptor has been proposed. The *SYM2* gene identified in certain ecotypes of pea (*Pisum sativum*) is a good candidate for such an entry receptor. We exploited the close phylogenetic relationship of pea and the model legume *Medicago truncatula* to identify genes specifically involved in rhizobial infection. The *SYM2* orthologous region of *M. truncatula* contains 15 putative receptor-like genes, of which 7 are LysM domain–containing receptor-like kinases (LYKs). Using reverse genetics in *M. truncatula*, we show that two LYK genes are specifically involved in infection thread formation. This, as well as the properties of the LysM domains, strongly suggests that they are Nod factor entry receptors.

The establishment of a nitrogen-fixing nodule symbiosis by rhizobial bacteria on the roots of legumes requires that the bacteria enter the root in a host-controlled manner. In most legumes, this infection starts with curling of root hairs. A bacterium becomes trapped in a cavity formed by the curl, where it forms a microcolony (1) (Fig. 1A). Infection thread formation is initiated within this cavity by invagination of the root-hair plasma membrane. In this way, a tubelike structure is formed by which the bacteria enter the plant and reach the base of the root hair

(Fig. 1B). Ultimately, the infection thread reaches a nodule primordium formed in the root cortex that develops into a nitrogen-fixing nodule upon release of the bacteria.

Rhizobia secrete specific lipochitoooligosaccharides, the so-called Nod factors, when they colonize the roots of their legume host. A Nod factor consists of a β-1,4-linked *N*-acetyl-D-glucosamine backbone of four or five residues, of which an acyl chain is attached at the C-2 position of the nonreducing terminal glucosamine residue (2). Depending on the rhizobial species, the structure of the acyl chain can vary, and substitutions at the reducing and nonreducing terminal glucosamine residues can be present (3). Nod factors are involved in induction of the early steps of nodulation and are also a major determinant of host specificity of nodulation.

Because responses are induced in the plant by Nod factor concentrations in a nano- to picomolar range, it seems probable that Nod factors are recognized by specific receptors (3–7).

Infection thread formation shows the highest demand toward Nod factor structure of all *Rhizobium*–induced responses (7–10). This has been studied in detail in the interaction of *Sinorhizobium meliloti* (*Sm*) and the model legume *Medicago truncatula* (7, 8). The *nodFnodL* mutant of *Sm* produces Nod factors that, in comparison to those secreted by wild-type bacteria, lack an acetate substitution at the nonreducing terminal glucosamine residue and in which the specific acyl chain of 16 C atoms containing two double bonds (C16:2) is replaced by vaccenic acid (C18:1). This *nodFnodL* mutant is able to induce most steps of the nodulation process (e.g., cortical cell activation and the formation of root hair curls in which bacteria form a microcolony), but the trapped bacteria are unable to induce infection thread formation. Therefore, it has been proposed that the induction of infection thread formation requires a highly specific Nod factor receptor, which was named the entry receptor (7, 8).

We used confocal laser scanning microscopy (CLSM) to analyze in more detail the stage at which infection thread formation is blocked when *M. truncatula* is inoculated with a *nodFnodL* mutant (*Sm* 2011Δ*nodF/nodL*::Tn5-GFP). Most (~80%) of the infections were blocked at the initiation of infection thread formation, because only microcolonies were formed. However, in about 20% of the cases, infection thread–like structures were initiated. However, instead of a continuous tube, a structure composed of tube- and sac-like structures was formed, the growth of

Laboratory of Molecular Biology, Department of Plant Sciences, Wageningen University, Dreijenlaan 3, 6703HA, Wageningen, Netherlands.

*To whom correspondence should be addressed. E-mail: ton.bisseling@wur.nl